# Deciphering the Role of Symmetry and Ligand Field in Designing Three-Coordinate Uranium and Plutonium Single-Molecule Magnets

Sourav Dey and Gopalan Rajaraman*

Read Online

ACCESS | 📊 Metrics & More | 📰 Article Recommendations | 🆂🅸 Supporting Information

**ABSTRACT:** Actinide single-molecule magnets (SMMs) have gained paramount interest in molecular magnetism as they offer a larger barrier height of magnetization ($U_{eff}$) reversal compared to the lanthanide analogue, thanks to their greater metal−ligand covalency. However, the reported actinide SMMs to date yield a relatively smaller $U_{eff}$ as there is no established design principle to enhance $U_{eff}$ values. To address this issue, we have employed *ab initio* CASSCF/CASPT2/NEVPT2 calculations to study a series of three-coordinate $U^{3+}$ and $Pu^{3+}$ SMMs. To begin with, we have studied two experimentally characterized $U^{3+}$ ion-field-induced SMMs, namely, planar $[U\{N-(SiMe_2{}^tBu)_2\}_3]$ (**1**) and pyramidal $[U\{N(SiMe_3)_2\}_3]$ (**2**) complexes reported earlier. Both the complexes were found to stabilize $m_J = |\pm 1/2\rangle$ as the ground state with a very strong quantum tunneling of magnetization (QTM), rendering them unsuitable for SMMs. Our calculations reveal that in the pyramidal geometry (such as in **2**), the energy of the $5f^26d^1$ state is lowered compared to the planar geometry (as in **1**), resulting in a slightly better SMM characteristic in the former. To unravel the effect of symmetry in magnetic properties, *ab initio* calculations were performed on two reported T-shaped complexes $[U(NSi^iPr_2)_2(I)]$ (**3**) and $[U(NHAr^{iPr6})_2I]$ (**4**, $Ar^{iPr6} = 2,6-(2,4,6-iPr_3C_6H_2)_2C_6H_3$). Quite interestingly, $m_J = |\pm 9/2\rangle$ is found to be the ground state for both the complexes with a blocking barrier exceeding 900 cm$^{-1}$. Furthermore, to decipher the effect of the transuranic element in magnetic anisotropy, *ab initio* calculations were extended to the Pu analogue of **2**, $[Pu\{N(SiMe_3)_2\}_3]$ (**5**), which yields a record-breaking blocking barrier of ~1933 cm$^{-1}$. Among the three-coordinate geometries studied, the pyramidal geometry was found to offer substantial magnetic anisotropy for $Pu^{3+}$ ions, while a T-shaped geometry is best suited for $U^{3+}$ ions. While the chosen theoretical protocols' overestimation of barrier height cannot be avoided, these values are still several orders of magnitude larger than the $U_{eff}$ values reported for any actinide SMMs and unveil a design principle for superior three-coordinate actinide-based SMMs.
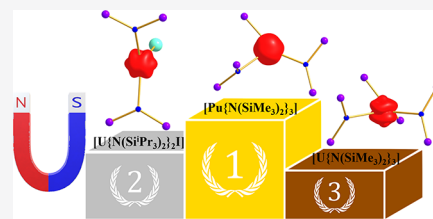
## 1. INTRODUCTION

Single-molecule magnets (SMMs) are of great interest in the field of molecular magnetism due to their potential application proposed in the area of information storage devices, molecular spintronics, and quantum computing.[1] The strong spin−orbit coupling induced by the deeply buried 4f orbital makes the lanthanide-based SMMs superior to transition metals on many counts.[2] In the past few years, the area has witnessed the discovery of novel lanthanide-based SMMs where the blocking temperature ($T_B$) has gone beyond liquid nitrogen temperatures.[2g,h,3] The axial limit of magnetic anisotropy has already been reached in these dysprocenium and related Dy(III) SMMs. Therefore, further enhancement of the blocking barrier ($U_{eff}$) is a challenging task in molecular magnetism.[3a−c] Moreover, the large $U_{eff}$ values are not translated to larger $T_B$ values due to various associated relaxation processes.[2b,3e,4] Recent studies show that both larger crystal field splitting and C−H vibrations are responsible for the enhancement of blocking temperature among the dysprocenium family of complexes, highlighting the need for a stronger crystal field to obtain higher $T_B$ values.[5]

In this regard, actinide-based SMMs have gained significant attention in the community of molecular magnetism[6] as the 5f orbitals of actinide interact strongly with the ligand field, which results in huge energy splitting of the crystal field states

compared to lanthanides, and in many cases, the gain in crystal field splitting in actinides is twice as much as Lanthanides.[7] The interest in the actinide complexes is driven by the scientific curiosity not only to grasp the fundamental chemistry of all of the elements in the periodic table but also to understand the reactivity, bonding, and electronic structure. This would be beneficial for the development of nuclear fuel cycles, waste remediation, and separation process that are vital for fulfilling global energy demands through nuclear power.[8] The first uranium-based SMM, $[U(Ph_2BPz_2)_3]$, was synthesized by Long et al. in 2009, containing a neutral diphenylbis(pyrazolylborate) ligand in which uranium resides in a trigonal prismatic geometry.[6a] Later, other uranium-based SMMs have been reported, most of them based on pyrazolylborate ligand.[6b,k,r,7,9] At the same time, the study of low coordinate (CN ≤ 4) actinide complex has gained significant attention in the past few years
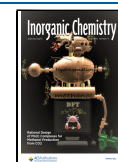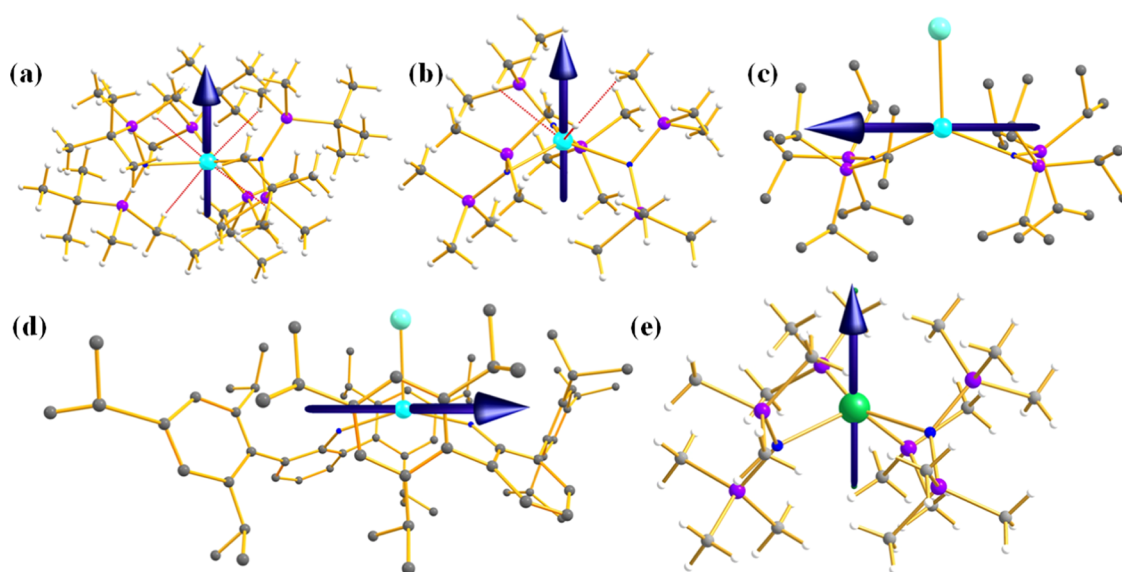
**Figure 1.** The $g_{zz}$ axis of KD1 for complexes (a) **1**, (b) **2**, (c) **3**, (d) **4**, and (e) **5**. Colour code: U, cyan; Pu, green; I, light cyan; Si, purple; N, blue; C, gray; and H, white. Hydrogens for complexes **3** and **4** are omitted for clarity.

due to their potential application in small-molecule activation along with the SMM behavior.[6f,t,u] The synthesis requires bulky ligands to prevent oligomerization due to large ionic radii of actinides, which do not prefer a low coordination number.[6u]

However, there are inherent challenges in actinide chemistry as it can be pursued only in selected laboratories due to the associated link with nuclear fuels.[8a,d−f,10] This has significantly hampered the development of actinide chemistry compared to lanthanide chemistry over the years. Theoretical tools based on *ab initio* methods played an essential role in the design and development of lanthanide-based molecular magnets. If potential targets are defined for actinide, this could help to spur the growth for this area. Unfortunately, theoretical studies of uranium-based SMMs are rare due to the intricacy involved in this chemistry and the need to assess and analyze the role of ligands in each of the examples due to the larger U-ligand covalency.[6h−j,l,m,11]

In this manuscript, we have investigated five experimentally characterized U(III)/Pu(III) complexes, $[U\{N(SiMe_2{}^tBu)_2\}_3]$ (**1**), $[U\{N(SiMe_3)_2\}_3]$ (**2**), $[U(NSi^iPr_2)_2(I)]$ (**3**), $[U-(NHAr^{iPr6})_2I]$ (**4**, $Ar^{iPr6}$ = 2,6-(2,4,6-$^iPr_3C_6H_2)_2C_6H_3$), and $[Pu\{N(SiMe_3)_2\}_3]$ (**5**), by *ab initio* CASSCF/RASSI-SO/SINGLE-ANISO calculations to assess and analyze, how geometry and ligand field influence the magnetic anisotropy (Figure 1).[6t,u,8a,12,13] Complexes **1** and **2** are field-induced SMMs with blocking barriers of 21.4 and 31 K, respectively, with a subtle difference in geometry. In this work, we aim to answer the following intriguing questions: (i) How important are the empty 6d orbitals of U/Pu(III) in estimating the magnetic anisotropy? (ii) Do the agostic Pu/U···H−$C_\gamma$ and $C_\gamma$−Si···U/Pu interactions observed in the X-ray structure influence the magnetic anisotropy? (iii) Between planar and pyramidal geometry, which suits the best for U(III)/Pu(III)? (iv) What are the best geometries for Pu(III)/U(III) that could yield a blocking barrier in the order of thousands of cm$^{-1}$ with a negligible QTM at the ground state?

## 2. COMPUTATIONAL DETAILS

The CASSCF/RASSI-SO/SINGLE_ANISO calculations have been performed using the MOLCAS 8.2 program package.[14] All

electron atomic natural type with relativistic core correlated (ANO-RCC) basis set was used for all calculations.[15] The following contraction scheme was used in the basis set: U: [U.ANO-RCC...10s9p7d5f3g2h.], Pu: [Pu.ANO-RCC...10s9p7d5f3g2h.], I: [I.ANO-RCC...6s5p3d1f.], N: [N.ANO-RCC...4s3p2d.], Si: [Si.ANO-RCC...4s3p1d.], C: [C.ANO-RCC...3s2p.], H: [H.ANO-RCC...2s.]. The Douglas−Kroll−Hess (DKH) Hamiltonian was used to take into account the relativistic effect.[16] To reduce the size of the disk space, Cholesky decomposition technique was employed.[17] The active space consists of three and five electrons in seven 5f orbitals (CAS(3,7) and CAS(5,7)) for U and Pu, respectively. Later, the active space was enlarged by including the 6d orbitals (CAS(3,12) and CAS(5,12) for U and Pu, respectively) to capture the nonbonding interaction and metal−ligand covalency of actinides. The dynamic correlation has been included by means of CAS(3,7)PT2 calculation. We have employed a standard IPEA shift of 0.25 for the CASPT2 calculations.[18] The 35 quartets and 112 doublets for uranium and 21 sextets, 224 quartets, and 490 doublets for plutonium were used in the CASSCF calculations (in complexes **1b**, **2′**, and **4**, the number of roots for quartets was increased to achieve the convergence). We have mixed the 35 quartets and 112 doublets of uranium; 21 sextets, 128 quartets, and 130 doublets for plutonium in the RASSI-SO module to calculate the energy of the spin−orbit states.[19] To compute the magnetic susceptibility, magnetization, and mechanism of relaxation pathways, the SINGLE_ANISO module of MOLCAS 8.2 was employed.[20]

On the other hand, we have also performed CASSCF/NEVPT2 (second-order N-electron valence perturbation theory) calculations using ORCA 4.0.1 programme package to estimate the spin−orbit coupling constant and magnetic susceptibility.[21] Here, we have used the basis set of SARC-DKH-TZVP for U, Sapporo-DKH3-DZP-2012 for I, DKH-def2-TZVP(-f) for N, and DKH-def2-SVP for the rest of the elements. The DKH Hamiltonian was used to take into account the scalar relativistic effects. The dynamic correlation is included by means of NEVPT2 in ORCA. The 35 quartets and 112 doublets were employed throughout the CASSCF/NEVPT2 calculations. The spin−orbit interaction was taken into account

**Table 1. Topological Parameters at the BCPs of U⋯H−C$_\gamma$ and U−N Bonds in 1 and 2[a]**

| | 1 | | | | | 2 | | | | |
|---|---|---|---|---|---|---|---|---|---|---|
| BCPs | $\rho(r)$ | $\nabla^2\rho(r)$ | $V(r)$ | $G(r)$ | $|V(r)|/G(r)$ | $\rho(r)$ | $\nabla^2\rho(r)$ | $V(r)$ | $G(r)$ | $|V(r)|/G(r)$ |
| U⋯H−C$_\gamma$ | 0.015 | 0.014 | 0.012 | 0.011 | 0.92 | 0.018 | 0.017 | 0.015 | 0.014 | 0.93 |
| | 0.013 | 0.012 | 0.011 | 0.010 | 0.91 | 0.018 | 0.017 | 0.016 | 0.014 | 0.87 |
| | 0.013 | 0.013 | 0.011 | 0.010 | 0.91 | 0.018 | 0.017 | 0.015 | 0.014 | 0.93 |
| | 0.013 | 0.014 | 0.012 | 0.011 | 0.92 | | | | | |
| U−N | 0.073 | 0.046 | 0.060 | 0.075 | 1.25 | 0.092 | 0.055 | 0.079 | 0.102 | 1.29 |
| U−N | 0.076 | 0.046 | 0.061 | 0.077 | 1.26 | 0.090 | 0.054 | 0.076 | 0.098 | 1.29 |
| U−N | 0.076 | 0.046 | 0.061 | 0.077 | 1.26 | 0.090 | 0.054 | 0.076 | 0.098 | 1.29 |

[a]$\rho(r)$ and $\nabla^2\rho(r)$ are given in the units of e$^-$/Å$^3$ and e$^-$/Å$^5$, respectively. $G(r)$ and $V(r)$ are shown in a.u.

by QDPT (quasi-degenerate perturbation theory) approach with SOMF (spin−orbit mean field) operator. The spin Hamiltonian (SH) parameters were estimated by EHA (effective Hamiltonian approach) formalism.[22] The crystal field parameters and $m_J$ composition of Kramers doublets depend on the orientation of a complex in the $\{X, Y, Z\}$ frame.[11,23] In this work, the Z-axis is chosen as the highest-order symmetry axis, while the choice of the X and Y axes is arbitrary.

Furthermore, single-point DFT calculations have been carried with UB3LYP functional in the Gaussian09 programme package.[24] All of the DFT calculations were performed without incorporating spin−orbit effects. We have used energy-consistent quasi-relativistic ECP60MWB pseudopotential (ECP) along with the ECP60MWB_ANO basis set for U and Pu, the TZVP basis set for Si and N, and the SVP basis set for C and H.[25,26] The topological analysis of the computed wave function was performed by AIM2000 programme package.[27]

We have analyzed all possible nonbonding interactions from donor Lewis-type NBOs to the acceptor non-Lewis NBOs by second-order perturbation theory.[28] The donor−acceptor stabilization energies ($\Delta E_{ab}$) are deduced from second-order perturbation theory as

$$\Delta E_{ab} = q_a \frac{F_{ab}^2}{\varepsilon_b - \varepsilon_a} \tag{1}$$

where $F_{ab}$ indicates the Fock matrix element on the basis of a and b NBO orbitals; $\varepsilon_a$ and $\varepsilon_b$ correspond to the energies of the donor and acceptor NBO orbitals; and $q_a$ denotes the donor orbital occupancy. The stabilization arises due to the electron delocalization from the donor to acceptor NBOs where the degree of delocalization determines the stabilization energy. The smaller the difference in energy between the donor and acceptor NBOs, the larger is the stabilization energy.[28]

## 3. RESULTS AND DISCUSSION

Complexes **1** and **2** are well characterized experimentally with the $^4I_{9/2}$ ground state (expected for a 5f$^3$ configuration) from their magnetic susceptibility data.[6t,u] Both the complexes display field-induced SMM behavior with a minimal blocking barrier. However, there is also a subtle difference in the electronic structure between **1** and **2**, evident from the electronic absorption spectrum.[6u] To fully comprehend all of these issues, we have first undertaken a detailed structural and bonding analysis of **1** and **2**.

**3.1. Electronic Structure, Bonding, and Magnetic Properties of Complexes 1 and 2.** The continuous shape measures (CShM) analysis on the X-ray structure using SHAPEv2.0 reveals that complexes **1** and **2** possess pseudo-$D_{3h}$ and $C_{3v}$ point groups, respectively (Table S1).[29] The U$^{3+}$ ion

in complex **1** has a trigonal planar environment with the average U−N bond distance of 2.403−2.415 Å, while the same in **2** is much smaller (2.311−2.325 Å), and this is likely due to the larger interligand repulsion in **1** (Figure 1) due to additional steric crowding.[6t,u] Complex **2** has a trigonal pyramidal geometry where the U$^{3+}$ ion lies 0.46 Å above the triangular plane formed by three less bulky trimethylsilyl amide ligands (Figure 1b). The average N−U−N bond angles are found to be 119.1−120.5° in **1**, while it is in the range of 115.9−116.4° in **2**. In addition to the U−N coordinate bond, U−C interactions are also detected in these structures, with the shortest U⋯C$_\gamma$/U⋯Si distances in **1** (**2**) found to be 3.12/3.43 Å (3.05/3.29 Å). Furthermore, we have also detected several U⋯H−C$_\gamma$ agostic interactions in complexes **1** and **2**, with the U⋯H distances lying in the range of 2.75−2.88 Å (see Figure 1). To find the intricate details of the U−N bond and U⋯H−C$_\gamma$ interactions observed in complexes **1** and **2**, we have undertaken topological and NBO analyses using DFT computed electron density of the spin-free ground state, although the actinide ions possess strong spin−orbit (SO) coupling. The topological analysis with the electron density from the SO-CASSCF or SO-CASPT2 method requires the inclusion of several ligand bonding and antibonding orbitals in the active space to capture the agostic-type interactions, which are beyond our computational limitation. Further, earlier topological studies on small actinide complexes with SO-CASSCF electron density yield very similar results to DFT, offering confidence in the bonding picture offered by the DFT methods.[30] Additionally, Bolvin and co-workers also showed that SO interaction has a minor effect on the bonding picture.[11]

*3.1.1. Topological and NBO Analysis of Bonding in 1 and 2.* In this section, we will compare the strengths of the metal−ligand interaction or metal−ligand covalency in complexes **1** and **2**. This will help us to analyze and probe the effect of the ligand field in magnetic anisotropy. In this regard, first, we have employed quantum theory of atoms in molecules (QTAIM) analysis to understand the nature of U−N bonds along with U⋯H−C$_\gamma$ interaction. The bonding and nonbonding interactions in QTAIM are represented by the critical points (CPs). There are four types of CPs (3, +3) (3, −1) (3, +1), and (3, −3) corresponding to the nuclear, bond, ring, and cage critical points.[31] The electron density ($\rho(r)$) at the BCP (bond critical point) of the U−N bond is found to be larger in **2** compared to **1** (Table 1). This is in accordance with the shorter average U−N bond distance in **2** compared to **1**. The diffused valence shell charge concentration (VSCC) in the contour plot of Laplacian of electron density ($\nabla^2\rho(r)$) implies that the metal−ligand interaction has a significant covalent contribution in both the complexes (Figure S1). The calculated $|V(r)|/G(r)$ ($G(r)$ is the kinetic energy density, $V(r)$ is the potential energy density) ratio is in the range of 1.25−1.29 also suggesting a significant covalent
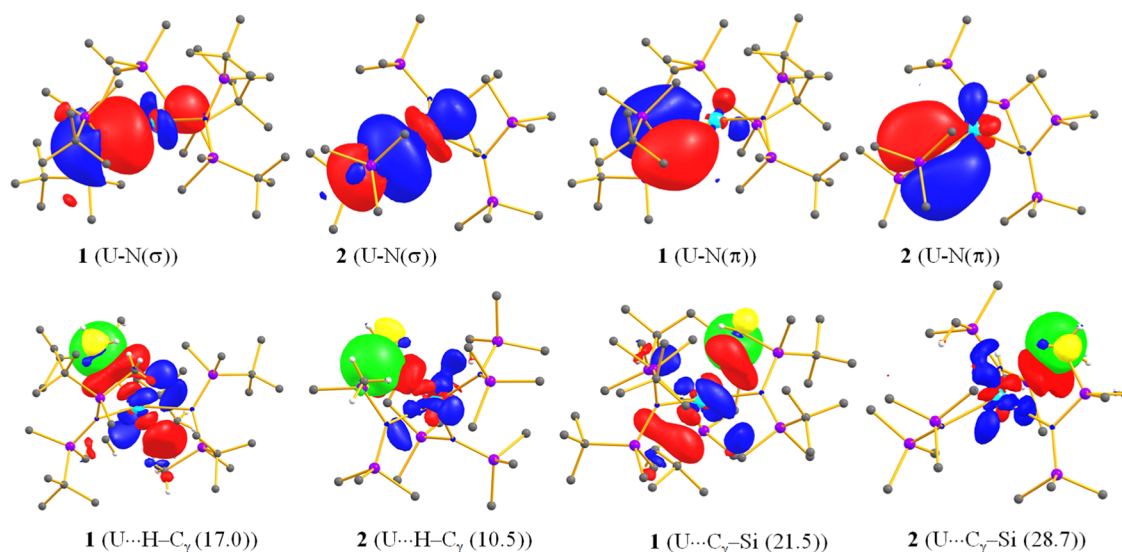
**Figure 2.** U−N ($\sigma$) and U−N ($\pi$) $\alpha$ NBO of complexes **1** and **2** (top). Color code: U, cyan; Si, purple; N, blue; C, gray; H, white. Here, red and blue colors denote the positive and negative isosurfaces, respectively, for an NBO orbital of uranium. The NBO orbitals have been shown with an isosurface value of 0.015 e$^-$/bohr$^3$. (Bottom) Donor−acceptor stabilization energy (kJ/mol) from $\sigma_{C\gamma-H}$ and $\sigma_{Si\gamma-C}$ to the 7s/7p/6d/5f hybrid empty orbitals ($\alpha$) of uranium. Here, the red(green) and blue(yellow) colors denote the positive and negative isosurfaces, respectively, for uranium (C−H and C−Si). Here the green-yellow lobe represents donor NBO and the red-blue isosurface represents acceptor NBO. Here, the NBO orbitals have been shown in an isosurface value of 0.05 e$^-$/bohr$^3$. The stabilization energy has been shown in parentheses (kJ/mol).

**Table 2. Computed Energies (cm$^{-1}$) of the Five Ground KDs (Three Ground KDs for Pu) of U along with g Tensor and $m_J$ Composition**

| energy | $g_x$ | $g_y$ | $g_z$ | $m_J$ composition | energy | $g_x$ | $g_y$ | $g_z$ | $m_J$ composition |
|---|---|---|---|---|---|---|---|---|---|
| **1**-CAS(3,7) | | | | | **2**-CAS(3,7) | | | | |
| 0.0 | 3.625 | 3.198 | 0.723 | $0.97|\pm 1/2\rangle$ | 0.0 | 3.581 | 3.075 | 0.629 | $0.97|\pm 1/2\rangle$ |
| 323.7 | 0.111 | 0.622 | 2.094 | $0.97|\pm 3/2\rangle$ | 211.7 | 0.226 | 0.267 | 1.879 | $0.95|\pm 3/2\rangle$ |
| 626.3 | 2.813 | 2.106 | 0.932 | $0.68|\pm 5/2\rangle + 0.30|\pm 7/2\rangle$ | 418.3 | 2.368 | 2.335 | 0.795 | $0.31|\pm 7/2\rangle + 0.57|\pm 5/2\rangle$ |
| 1293.5 | 2.730 | 2.628 | 2.285 | $0.69|\pm 7/2\rangle + 0.29|\pm 5/2\rangle$ | 1286.0 | 2.670 | 2.607 | 2.194 | $0.68|\pm 7/2\rangle + 0.30|\pm 5/2\rangle$ |
| 1659.2 | 0.023 | 0.045 | 6.026 | $0.98|\pm 9/2\rangle$ | 1569.9 | 0.019 | 0.029 | 5.826 | $0.95|\pm 9/2\rangle$ |
| **1a**-CASPT2 | | | | | **2a**-CASPT2 | | | | |
| 0.0 | 3.74 | 3.42 | 0.75 | $0.98|\pm 1/2\rangle$ | 0.0 | 3.81 | 3.14 | 0.66 | $0.97|\pm 1/2\rangle$ |
| 313.5 | 0.04 | 0.33 | 1.97 | $0.96|\pm 3/2\rangle$ | 242.04 | 0.15 | 0.43 | 1.78 | $0.93|\pm 3/2\rangle$ |
| 665.3 | 2.75 | 2.52 | 1.02 | $0.69|\pm 5/2\rangle + 0.30|\pm 7/2\rangle$ | 520.47 | 2.63 | 2.45 | 0.85 | $0.68|\pm 5/2\rangle + 0.31|\pm 7/2\rangle$ |
| 1159.0 | 0.05 | 0.07 | 6.15 | $0.96|\pm 9/2\rangle$ | 1059.23 | 0.20 | 0.35 | 5.76 | $0.93|\pm 9/2\rangle$ |
| 1244.4 | 2.86 | 2.71 | 2.37 | $0.69|7/2\rangle + 0.30|\pm 5/2\rangle$ | 1109.07 | 2.20 | 2.53 | 3.04 | $0.68|\pm 7/2\rangle + 0.30|\pm 5/2\rangle$ |
| **1**-CAS(3,12) | | | | | **2**-CAS(3,12) | | | | |
| 0.0 | 3.590 | 3.195 | 0.737 | $0.98|\pm 1/2\rangle$ | 0.0 | 3.623 | 2.987 | 0.702 | $0.98|\pm 1/2\rangle$ |
| 360.9 | 0.105 | 0.582 | 2.100 | $0.97|\pm 3/2\rangle$ | 315.1 | 0.290 | 0.337 | 1.895 | $0.95|\pm 3/2\rangle$ |
| 715.6 | 2.736 | 2.076 | 1.045 | $0.70|\pm 5/2\rangle + 0.29|\pm 7/2\rangle$ | 609.1 | 2.411 | 2.377 | 0.837 | $0.68|\pm 5/2\rangle + 0.31|\pm 7/2\rangle$ |
| 1531.8 | 2.694 | 2.582 | 2.374 | $0.70|\pm 7/2\rangle + 0.28|\pm 5/2\rangle$ | 1693.7 | 2.699 | 2.612 | 2.175 | $0.68|\pm 7/2\rangle + 0.30|\pm 5/2\rangle$ |
| 1918.2 | 0.023 | 0.047 | 6.192 | $0.98|\pm 9/2\rangle$ | 1962.4 | 0.025 | 0.049 | 5.811 | $0.96|\pm 9/2\rangle$ |
| Exp (**1**) | 3.55 | 2.97 | 0.55 | | | | | | |
| **5**-CAS(3,12) | | | | | **5′** (3,12) | | | | |
| 0.0 | 0.093 | 0.096 | 0.945 | $0.98|\pm 5/2\rangle$ | 0.0 | 0.162 | 0.164 | 0.901 | $0.98|\pm 5/2\rangle$ |
| 1232.3 | 0.003 | 0.005 | 0.114 | $0.99|\pm 3/2\rangle$ | 1280.6 | 0.001 | 0.006 | 0.322 | $1.00|\pm 3/2\rangle$ |
| 1933.3 | 1.118 | 1.104 | 0.037 | $0.98|\pm 1/2\rangle$ | 2252.0 | 1.036 | 1.030 | 0.038 | $0.98|\pm 1/2\rangle$ |

contribution to the metal−ligand bond (Table 1, $|V(r)|/G(r)| <$ 1—completely ionic and $|V(r)|/G(r)| > 2$—completely covalent[32]) in both the complexes. Interestingly, the values computed for complexes **1** and **2** indicate stronger metal−ligand covalency than their Er−N counterpart studied earlier,[33] affirming covalent actinide−ligand interaction compared to ionic lanthanide−ligand interaction.

For the nonbonding interactions, QTAIM analysis reveals the presence of four and three (3, −1) BCPs between U and H−C$_\gamma$

for complexes **1** and **2**, respectively, confirming the agostic interaction hypothesized based on the X-ray structure (see molecular graphs in Figure S2). The very small and positive $\rho(r)$ and $\nabla^2\rho(r)$ values at those critical points indicate that the interaction is of closed-shell type (Table 1). Furthermore, the $|V(r)|/G(r)$ ratio at these BCPs is less than 1, also suggesting the ionic character of the U···H−C$_\gamma$ interaction (Table 1).[32,34] However, the more diffused VSCC unveils stronger agostic interaction in **2** than **1** (Figure S3). The computed $\rho(r)$ reveals
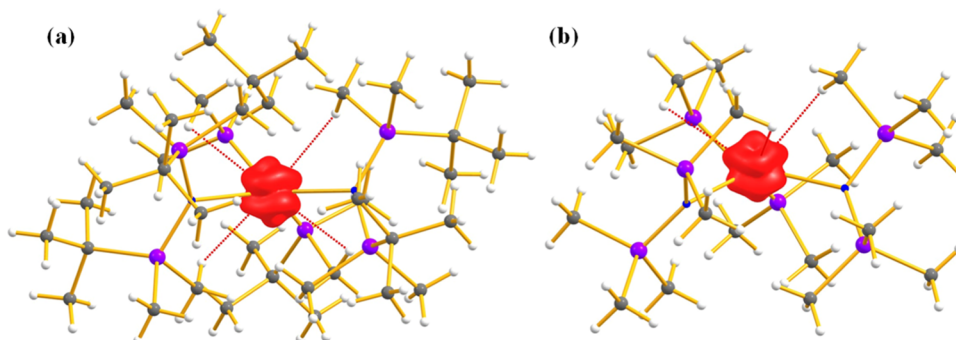
**Figure 3.** $\alpha$ Electron density (isosurface value = 0.06 e$^-$/bohr$^3$) of ground spin free state in complexes **1** (a) and **2** (b). Red dotted lines represent the U···H−C$_\gamma$ agostic interactions. Color code: U, cyan; Si, purple; N, blue; C, gray; H, white.
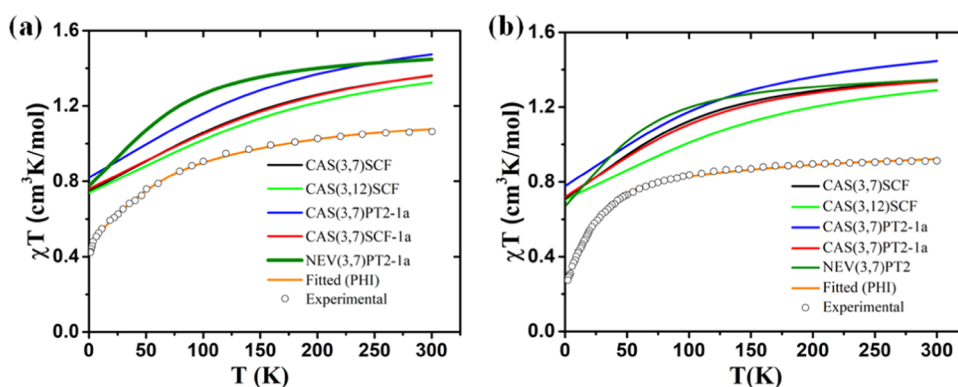


**Figure 4.** Comparison of temperature-dependent magnetic susceptibility with experiments of (a) **1** and (b) **2**.

that the agostic interaction is ∼1/5th of the U−N bond strength and suggests that all of the agostic interactions put together approximately add crystal field strength equivalent to one U−L bond altering the simple geometrical perspective established based on coordinate covalent bonds.

Further, to quantify the metal−ligand covalency and the stabilization energy from the agostic interaction, we have undertaken NBO analysis. Such analysis can unveil the nature of the orbitals involved in agostic-type interactions and how these can alter the magnetic anisotropy. The NBO analysis reveals the presence of one $\sigma$ and one $\pi$ for each U−N bond in **1** and **2** (see Tables S2 and S3 and Figure 2). While both types of bonds are found to be ionic, the U−N $\sigma$ bond in **1** is found more ionic than that of **2** (see Tables S2 and S3). The U−N bond is formed from the 7s/7p/6d/5f hybrid orbital of uranium, where the 6d orbital contributes significantly to the bonding compared to others (Figure 2, Tables S2 and S3). More importantly, U is found to have sp$^{1.02}$d$^{11.77}$f$^{7.71}$ hybridization (for U−N($\sigma$)) in **1**, while in **2**, the hybridization is found to be sp$^{0.66}$d$^{7.77}$f$^{3.72}$, showing a significant drop in the d-orbital contribution as we move from planar (**1**) to pyramidal (**2**) with a concomitant increase in the f-orbital contribution. On the other hand, for the $\pi$-bonds, a reverse scenario is noted, with a strong d-contribution for the pyramidal and stronger f-contribution to the planar structure.

NBO second-order perturbation theory donor−acceptor analysis reveals stronger C$_\gamma$−H···U agostic interaction in **1** (17.0 kJ/mol) than in **2** (10.5 kJ/mol, see Figure 2), which does corroborate with their corresponding distances. This suggests the favorable orientation of the 6d orbital toward the C$_\gamma$−H···U agostic interactions in planar compared to the pyramidal geometry. On the other hand, in pyramidal geometry, the C$_\gamma$−Si···U agostic interactions are stronger than that in planar

(Figure 2 and Tables S4 and S5 in the Supporting Information). Furthermore, the total stabilization energy by summing over the contributions from several weaker agostic interactions (only interactions with stabilization energy >8 kJ/mol are shown in Tables S4 and S5) is found to be larger in **1** than in **2**. This is likely to be one of the reasons for the planarity of complex **1**, while the three-coordinate actinide complexes prefer pyramidal geometry.

*3.1.2. Assessing the Role of CASSCF Active Space in Reproducing Experimental Susceptibility Data for Complexes 1 and 2.* Experimental studies reveal that complexes **1** and **2** behave as field-induced SMMs with the estimated $U_{eff}$ values of 14.9 and 21.5 cm$^{-1}$ in an applied dc field.[6t,u] Further, X- and Q-band EPR studies were undertaken in complex **1** that yield g-tensors $g_{eff}$ = 3.55, 2.97, and 0.553. The difference in the blocking barrier suggests the role of geometry on the magnetic properties. To further understand the origin of this difference, *ab initio* SA-CAS(3,7)SCF/RASSI-SO/SINGLE_ANISO calculations were performed using MOLCAS 8.2 suite.[14] The calculations on **1** (**2**) reveals a very strong transverse anisotropy $g_x$ = 3.625; $g_y$ = 3.198; $g_z$ = 0.723 ($g_x$ = 3.581; $g_y$ = 3.075; $g_z$ = 0.629; Table 2) in the ground state and the computed g-tensors are in good agreement with the experiments. The five Kramers doublets (KDs) generated from $^4I_{9/2}$ state in **1** (**2**) span up to 1659.2 (1569.9) cm$^{-1}$ (Table 2). The $g_{zz}$ axis of KD1 is found to be oriented along the highest-order symmetry axis in both the complexes (Figures 1 and S4). We have also shown the 5f orbital splitting of the ground quartet state based on the approximate point group symmetry they belong to (Figures S5 and S6). The 5f orbitals are found to split into $E' + A_2'' + A_1' + E'' + A_2'$ and $A_1 + E + A_1' + E' + A_2$ irreducible representation in **1** and **2**, respectively. This splitting pattern is in accordance with the

pseudo-$D_{3h}$ and $C_{3v}$ point groups for **1** and **2**, respectively. The mechanism of magnetization relaxation developed for **1** and **2** unveils a strong QTM in the ground state due to the stabilization of the lowest $m_J = |\pm 1/2\rangle$ as the ground state (Figure S7). The strong QTM is also indicated by the positive value of the computed $B_2^0$ crystal field parameter (see Table S6). This results in the prolate-type ground electron density of $U^{3+}$ in complexes **1** and **2** (Figures 3, S8, and S9) and rules out any possibility for zero-field SMM behavior, which is in accordance with the experiment. The first excited KD of **1** (**2**) at 323.7 cm$^{-1}$ (211.7 cm$^{-1}$) is found to possess a significant contribution from $m_J = |\pm 3/2\rangle$ (Table 2, Figure S7).

The temperature-dependent magnetic susceptibility ($\chi T$) computed for **1** and **2** are shown along with experimental data in Figure 4. The calculated values are much higher than the experimental value suggesting overestimation of the crystal field parameters by the *ab initio* methods. This may be attributed to the minimal reference space chosen, and unlike Lanthanides, where Ln-ligand bonding is strongly ionic, the U-ligand bonds exhibit a certain amount of covalency.[6h−j,l,m] This demands the inclusion of other orbitals in the reference space. Particularly the 4f−5d gap in lanthanides is huge (ca. 12.0 eV),[35] while the 5f−6d gap is relatively small in actinides (ca. 2.0 eV).[6h,u] Therefore, the 6d orbitals are expected to play a critical role in the accurate determination of crystal field parameters (see Figure 5).
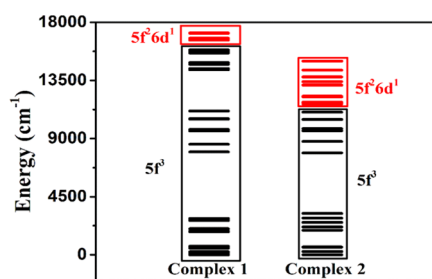


**Figure 5.** CAS(3,12)SCF-computed energies of 35 quartets in complexes **1** and **2**. Black and red horizontal lines represent the 5f$^3$ and 5f$^2$6d$^1$ states of $U^{3+}$, respectively.

Further to assess the importance of reference space in reproducing susceptibility data, calculations were performed with the inclusion of dynamic correlation via CASPT2 methods. As these are computationally demanding, models **1a** and **2a** were carved out from **1** and **2** by substituting bulky alkyl groups with hydrogen atoms (see Figure S10 for the $g_{zz}$ axis of KD1). The CASSCF/RASSI-SO/SINGLE_ANISO calculation with CAS-(3,7) active space on **1a** and **2a** reveals a similar set of energy values and $g$ tensors (Tables S7 and S8) and $\chi T$ (Figure 4). This enables us to perform the CAS(3,7)PT2 calculation on models **1a** and **2a**. The energy splitting as well as the energy gap between KD1-KD2 of **1** and **2** decrease significantly with the inclusion of dynamic correlation by CAS(3,7)PT2 (Table 2). However, CAS(3,7)PT2-computed $g$ tensors and the temperature-dependent magnetic susceptibility are not in agreement (Table 2 and Figure 4) with the experiments. Further, CAS(3,7)SCF/NEVPT2 calculations were performed on **2** (also on model **1a**), and this also yields susceptibility data that deviate from the experiment (Figure 4). The NEVPT2-computed energy of the KD2 becomes smaller than the computed with CASPT2, although the energy splitting of five KDs is higher in the former (Tables 2, S9, and S10). On the other hand, the NEVPT2-computed $g$ factors of KD1 show

closer agreement with the experiment than those calculated with CASPT2 for **1a**. However, the inclusion of dynamic correlation via CASPT2/NEVPT2 calculations is not well suited to reproduce the experimental $\chi T$ data compared to CASSCF methods in actinide complexes, and this has also been observed in earlier examples.[6h,j,l,m]

Another way to capture the metal−ligand covalency is to increase the active space size, and earlier studies on $[U(NH_2)_3]$ model reveal that pyramidalization lowers the energy of the 5f$^2$6d$^1$,[36] which lies ca. 2000 cm$^{-1}$ above the 5f$^3$ states. For these reasons, the active space has been enlarged to CAS(3,12) from CAS(3,7), including 6d orbitals of $U^{3+}$ ion. This extended reference space was found to lower the computed susceptibility (see Figure 4) compared to other active spaces and also yielded a 5f$^3$ → 5f$^2$6d$^1$ gap of ~ca. 16 611 cm$^{-1}$ for **1** (Figure 5), which is also qualitatively in agreement with experiments (~22 000 cm$^{-1}$ from Luminescence data).[6u] Further, this 5f$^3$ → 5f$^2$6d$^1$ gap has been shown to decrease with an increase in pyramidalization (Figure 5, 21 500 cm$^{-1}$ for $[U\{N(SiPhMe_2)_2\}_3]$[37] with a pyramidal shift of 0.87 Å), and this is also consistent with the estimate obtained for complex **2** (11 665 cm$^{-1}$).

The incorporation of 6d orbitals in the reference space improves the results better compared to the perturbative corrections (Table 2 and Figure 4) for the following reasons: (i) the 6d orbitals are strongly diffused, allowing strong delocalization of spins, and this is apparent from lowering of 5f$^2$6d$^1$ gap; (ii) the 6d orbitals also participate in the U−N bonds (Figures S11 and S12) and hence has a large N contribution, capturing some effect of U−N $\sigma/\pi$ bonds; (iii) the agostic interactions are approximately equivalent to one U−L bond strength and inclusion of which directly capture these effects.[6l,m] Therefore, we have used CAS($n$,12) ($n$ = number of 5f electrons) active space in all of the subsequent calculations. However, the CAS(3,12)SCF/RASSI-SO/SINGLE_ANISO calculation reveals the enhancement of the energy splitting of the five KDs (1918.2 and 1962.4 cm$^{-1}$ for **1** and **2**, respectively) as well as the energy gap between KD1 and KD2 in both complexes **1** and **2** (Table 2) compared to CAS(3,7) results.

*3.1.3. Fitting the Experimental Magnetic Susceptibility Using Ab Initio Computed Crystal Field Parameters.* The CAS(3,12)SCF-computed $\chi T$ data of both **1** and **2** are still overestimated compared to experiments (Figure 4). As a further expansion of CAS reference space is computationally demanding, we have attempted to fit the experimental $\chi T$ using computed crystal field (CF) parameters $B_k^q$, using PHI suite with the CAS(3,12)SCF calculated results as a priori.[3b,38] Since complexes **1** and **2** possess pseudo-$D_{3h}$ and $C_{3v}$ symmetry, respectively, the following spin Hamiltonian was employed during the fitting of magnetic susceptibility of **1** (eq 2) and **2** (eq 3).[39]

$$\hat{H}_{CF} = B_2^0 O_2^0 + B_4^0 O_4^0 + B_6^0 O_6^0 + B_6^6 O_6^6 \tag{2}$$

$$\hat{H}_{CF} = B_2^0 O_2^0 + B_4^0 O_4^0 + B_4^3 O_4^3 + B_6^0 O_6^0 + B_6^0 O_6^3 + B_6^6 O_6^6 \tag{3}$$

The spin−orbit coupling constant ($\lambda$) employed in the fitting has been estimated from the CASSCF calculations with ORCA 4.0.1 program package (585 cm$^{-1}$ for **1** and 576.4 cm$^{-1}$ for **2**, see Table S11).[40] To take into account the short intermolecular distance (9.028 and 10.327 Å in **1** and **2**, respectively), the intermolecular interaction ($zJ$) of −0.1 cm$^{-1}$ was also considered. Additionally, a small TIP (temperature-independent paramagnetism) of −0.0015 (−0.001) for **1** (**2**) was used to
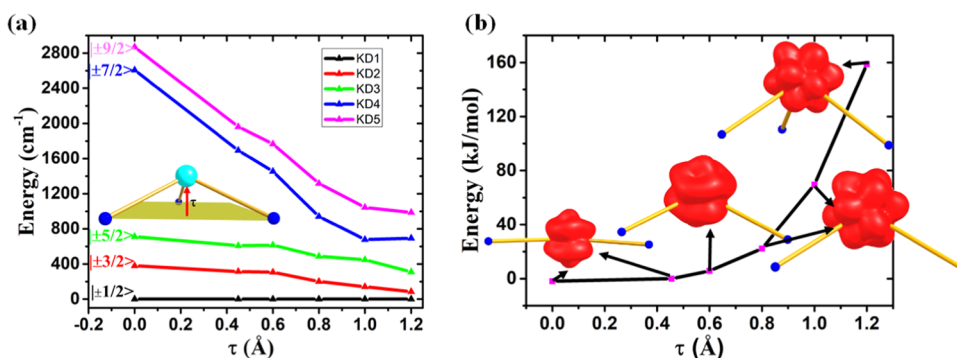
**Figure 6.** (a) Energy of the five ground KDs of complex **2** with the $\tau$ value. (b) Change in the single-point energy (computed by DFT) with $\tau$ value. The $\alpha$ electron density of the ground spin free state with the $\tau$ value has been shown with an isosurface value of 0.06 e⁻/bohr³. All other coordinated atoms except nitrogens have been removed for clarity. Color code: U, cyan; N, blue.
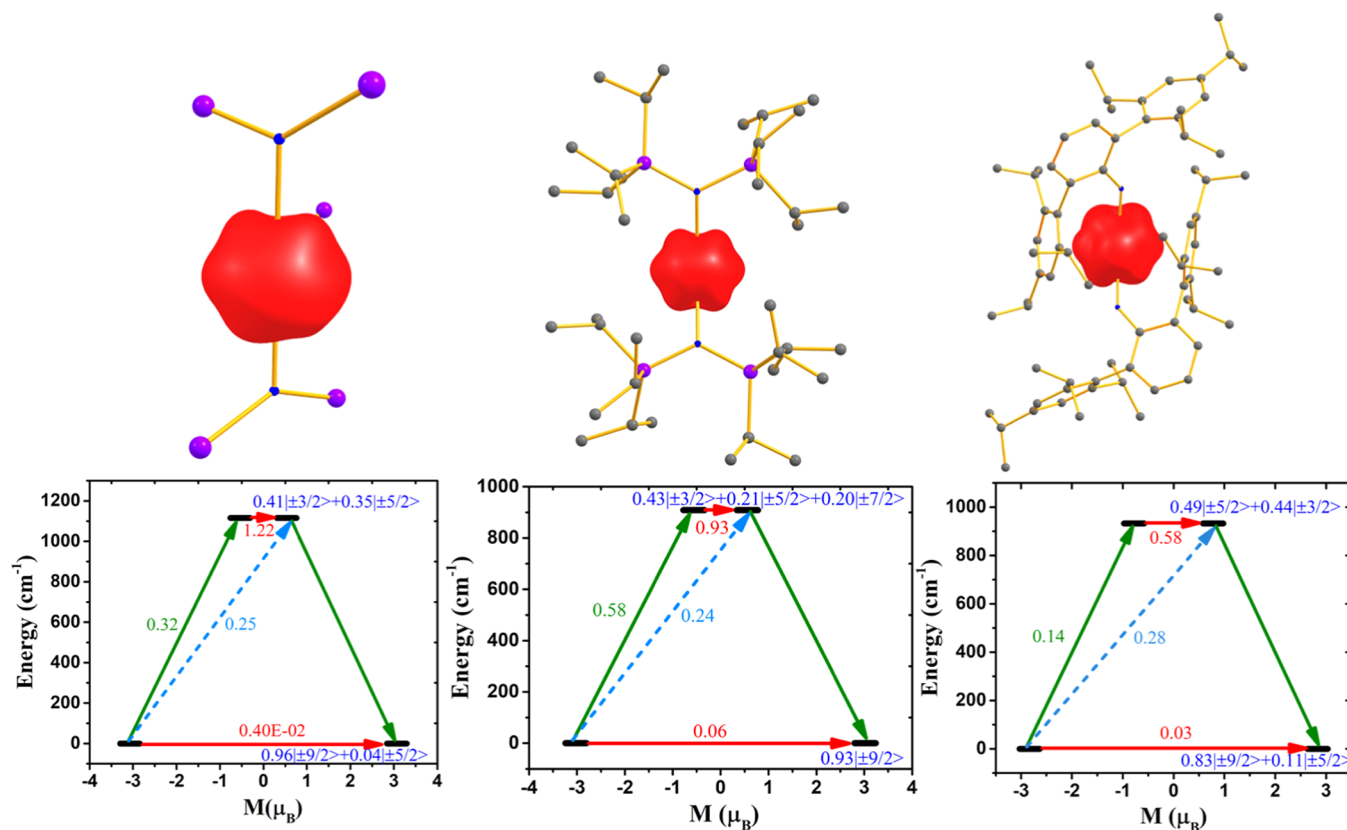


**Figure 7.** $\alpha$ Electron density (with isosurface value of 0.06 e⁻/bohr³) of the ground spin free state in **1b** (top left), **3** (top middle), and **4** (top right). Color code: U, cyan; Si, purple; N, blue; C, gray. Hydrogens are omitted for clarity. The mechanism of magnetic relaxation has been shown below each corresponding complex. The red arrows indicate the QTM and TA-QTM via ground and higher excited KD, respectively. The sky-dotted arrows show the Orbach process for relaxation. The green arrows represent the mechanism of magnetic relaxation. The blue characters imply the $m_J$ composition of the KDs.

account for the significant contribution that arises from the $^2H_{9/2}$ first excited J state as shown earlier.[6t,u,41] Both the zJ and TIP values are independently varied in the initial simulations to arrive at the best estimate as given above, and these values were then fixed at the final fitting of CFPs. It is noteworthy to mention that similar zJ and TIP were employed in the fitting of experimental $\chi T$ data of uranium complexes by Coronado and co-workers.[41] However, the fitted CF parameters are found to be smaller than the computed values. Particularly, the $B_2^0$ CF parameter is ca. 7 (4) times smaller compared to the CAS(3,12)SCF results for complex **1** (**2**) (Table S11 and Figure 4). This suggests that the anisotropy as well the CF

parameters for the actinides are overestimated in the *ab initio* methodology. It is important to note that the equivalent lanthanide ion, Nd(III), also has similar problems.[42] This suggests that for less than half-filled 4f/5f elements, over-estimation of CF parameters/anisotropy is inherent with this methodology, and the expansion of reference space further perhaps using methods such as DMRG could provide a solution.[42,43]

**3.2. Magneto-Structural Correlation on 2.** The uranium atom resides ca. 0.456 Å out the plane ($\tau$) formed by the three-silyl amide ligand in **2**, which gives rise to the lowering of KD1−KD2 energy gap as well as energy splitting of the five KDs (see

CAS(3,7) computed energies of **1** and **2**, Table 1) compared to **1**. Therefore, we have performed a magneto-structural correlation by varying the $\tau$ value in **2** from 0.0 (**2′**) to 1.2 Å. The $\tau$ value among the magneto-structural points was varied by moving the U ion from the plane, and no further structural minimization was carried out. The *ab initio* CAS(3,12)SCF/ RASSI-SO/SINGLE_ANISO calculation reveals a decrease in the KD1−KD2 energy gap as well as the energy splitting of the five ground KDs (KD1−5 of **2** corresponds to dominant $m_J = |$ $\pm1/2\rangle$, $|\pm3/2\rangle$, $|\pm5/2\rangle$, $|\pm7/2\rangle$, and $|\pm9/2\rangle$ states, Table S12 and Figure 6a) with an increase in $\tau$ value as this diminishes the metal−ligand interaction. Further, as the $\tau$ value increases, the ground $m_J = |\pm1/2\rangle$ contribution to the ground state decreases with a concomitant increase of contribution from higher $m_J$ levels. This results in the reduction of ground-state prolicity (Figure 6b). The energy window of the out-of-plane correlation is 160 kJ/mol, and therefore, moderate alteration of $\tau$ value is feasible (Figure 6b). However, the ground-state transverse anisotropy does not alter significantly with the $\tau$ values. The ground-state QTM, for this reason, remains stronger across all of the points studied, rendering zero-field SMM impossible by altering the $\tau$ value alone. Overall, the magneto-structural correlation reveals the crystal field splitting and ground $m_J$ is strongly sensitive to the $\tau$ value compared to the lanthanides.[33]

**3.3. Effect of Symmetry on Magnetic Properties.** Since the computed $g$ tensor and the energy of the five KDs of **1a** is similar to **1**, we have further modelled a T-shaped complex ($C_{2v}$ symmetry) **1b** from model **1a** to find out the effect of all possible three-coordinate geometries on magnetization relaxation (see Figures 1, 7, and S13). The CAS(3,12)SCF/RASSI-SO/ SINGLE_ANISO calculations on model **1b** reveal negligible transverse anisotropy ($g_x = 0.011$; $g_y = 0.013$; $g_z = 6.138$) of KD1 (Tables S13 and S14), which results in a tiny QTM value (0.004 $\mu_B$) and quite interestingly $m_J = |\pm9/2\rangle$ is stabilized as the ground state (Tables S13 and S14 and Figure 7). The negative sign of the computed $B_2^0$ CF parameter indicates the presence of large axiality on this complex (Table S15). The 5f orbitals are found to split into $B_2 + A_1 + B_1 + A_1' + A_2 + B_2' + B_1'$, irreducible representation as per the $C_{2v}$ symmetry present in the molecule (Figure S14). A significant TA-QTM (1.22 $\mu_B$) in the KD2 due to large transverse anisotropy reinforces magnetization relaxation via this state (Figure 7), and this results in a very large $U_{cal}$ value of 1116 cm$^{-1}$, which is ca. 40 times higher than the $U_{eff}$ value reported for the best U(III) SMMs.[6b,k,44] As expected for this geometry, an oblate electron density is detected at the spin-free ground state contrary to the prolate one observed for **1** and **2** (Figures 3 and 7). The result implies that fine-tuning the symmetry of three-coordinate U(III) complexes is the key to enhance blocking barriers.

Furthermore, to authenticate the remarkable results observed on model **1b**, we have performed *ab initio* CAS(3,12)SCF/ RASSI-SO/SINGLE_ANISO calculations on two U$^{3+}$ complexes reported earlier possessing T-shaped geometry (see Figures 7 and S13), [U(NSi$^i$Pr$_2$)$_2$(I)] (**3**) and [U(NHAr$^{iPr6}$)$_2$I] (**4**, Ar$^{iPr6}$ = 2,6-(2,4,6-$^i$Pr$_3$C$_6$H$_2$)$_2$C$_6$H$_3$).[13a,45] Both complexes **3** and **4** were characterized by dc susceptibility and EPR spectroscopy but lack ac susceptibility data. Complex **3** (**4**) exhibits two well-resolved peaks at $g_{eff}$ values of 4.9 (5.2) and 3.3 (4.6) in the EPR spectra, and the $\chi T$ value (Figure S15) does not go beyond 0.76 cm$^3$ kmol$^{-1}$ at 2 K (while it was 0.41 and 0.27 cm$^3$ kmol$^{-1}$ for **1** and **2**, respectively, at 2 K). This suggests the extensive contribution of ground KD from the higher $m_J$ states. The ground-state easy axis (from *ab initio* calculation) of **3** and **4**

lies along with the N−U−N plane due to the weak iodide ligand in the equatorial position (Figures 1 and S13). The *ab initio* CAS(3,12)SCF calculations on **3** and **4** reveal very small transverse anisotropy in the ground KD (**3**: $g_x = 0.139$; $g_y = 0.203$; $g_z = 6.039$, **4**: $g_x = 0.133$; $g_y = 0.118$; $g_z = 5.574$, Tables S16−S19), and it is reflected in the negligible QTM computed (Tables S16−S19 and Figure 7). For these complexes, a $m_J = |\pm9/2\rangle$ is stabilized as the ground state, which leads to an oblate shape electron density for the ground state (Figure 7) as expected based on model **1b**. The negative sign of the computed $B_2^0$ CF parameter in **3** and **4** suggests the large axiality on these complexes (Table S15). However, a significant TA-QTM in the first excited KD reinforces the magnetization relaxation via this state due to substantial mixing of $m_J = |\pm3/2\rangle$ and $|\pm5/2\rangle$ states (Figure 7). This results in a huge $U_{cal}$ value of 908.4 and 932.3 cm$^{-1}$ for complexes **3** and **4**, respectively. The temperature-dependent magnetic susceptibility data obtained from CAS(3,7) and CAS(3,12) calculations show deviation from the experimental data (Figure S15). Therefore, we have attempted to fit the experimental $\chi T$ by varying the *ab initio* computed CF parameters (nonvanishing $B_k^q$: $B_2^0$, $B_2^2$, $B_4^0$, $B_4^2$, $B_4^4$, $B_6^0$, $B_6^2$, $B_6^4$, $B_6^6$) considering $C_{2v}$ symmetry for T-shaped geometry.[39] The spin−orbit coupling ($\lambda$) in the fitting has been obtained from the CASSCF calculations performed with ORCA as mentioned earlier (589 cm$^{-1}$ for **3** and 580.6 cm$^{-1}$ for **4**, see Table S20). The fitted axial $B_2^0$ crystal field parameter (Table S20 and Figure S15) are found to be 1.07 times smaller (4.54 times larger) compared to the computed one for **3** (**4**), and this infers that the very large blocking barriers are a reality for both these complexes and unveils that T-shaped geometry should be preferentially targeted for futuristic U$^{3+}$ SMMs.

**3.4. Magnetic Anisotropy of Pu(III) SMMs.** Transuranic compounds are also of fundamental interest, particularly plutonium, which appears in nuclear waste and is hard to recycle ($\sim$4% cannot be recycled), and any possible usage of this would be beneficial for nuclear waste management, an area actively under development.[8] Moreover, the extent of participation of 5f and 6d orbitals beyond uranium has not been established.[46] Later, actinides like plutonium display fascinating chemistry with all of the possible oxidation states (III−VII) and have been less explored compared to uranium due to the high radioactivity of available isotopes.[6j,47] In this regard, Neu and co-workers have reported a rare low coordinate plutonium complex Pu[N(SiMe$_3$)$_2$]$_3$ (**5**, Figure 1) analogous to **2**.[8a] The Pu−N distance in **5** is reported to be around 2.313 Å, which is shorter compared to the U−N distance in **2**. The Pu atom in **5** is found to have $\sim$0.579 Å out-of-plane $\tau$ parameter. The N−Pu−N bond angles are found to be slightly shorter ($\sim$114.0°) in **5** compared to **2**. The Pu⋯C$_\gamma$ bond distances are found to be 2.968 Å, suggesting the presence of strong agostic interaction between Pu(III) and C$_\gamma$−H, C$_\gamma$−Si. QTAIM analysis in complex **5** suggests three BCPs (see Figure S16) between Pu(III) and C$_\gamma$−H atom, and this is similar to **2**. The $|V(r)|/G(r)$ ratio at these BCPs are smaller than **2** (Table S21), suggesting weaker agostic interactions compared to complexes **1** and **2** (see the $\nabla^2\rho(r)$ plot in Figure S17). But the agostic interaction between Pu and C$_\gamma$−Si becomes stronger compared to **1** and **2** with the involvement of low-lying 7p orbitals of plutonium (see Figure S18 and Tables S22 and S23). The lesser covalency of the Pu−N bond compared to U−N bonds in **1** and **2** is also confirmed by the $|V(r)|/G(r)$ ratio and VSCC in the Laplacian of electron density. The NBO analysis (Tables S22 and S23, Figure S18) also suggests a smaller contribution from Pu in Pu−
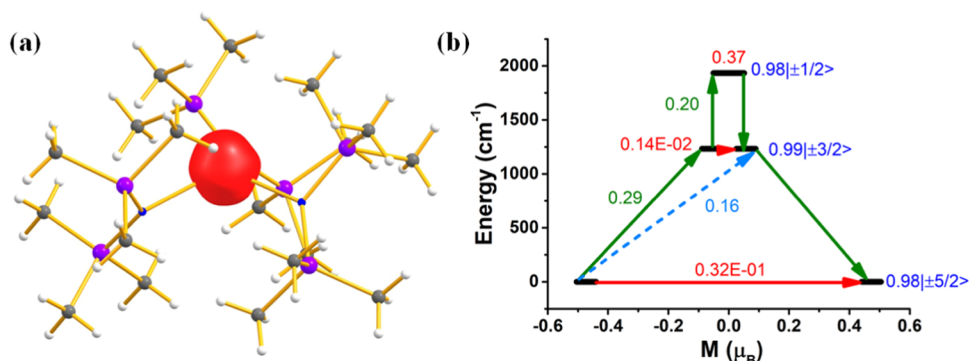
**Figure 8.** (a) $\alpha$ Electron (isosurface value 0.06 e$^-$/bohr$^3$) density of the ground spin free state in **5**. (b) Mechanism of magnetic relaxation of **5**. Red arrows indicate the QTM and TA-QTM via ground and higher excited KD, respectively. The sky-dotted arrows represent the Orbach process for relaxation. Olive arrows show the mechanism of magnetic relaxation. Blue characters imply the $m_J$ composition of the KDs.

N bonding than the U—N bond in **2**. It is noteworthy to mention that the Pu—N $\pi$ bond (from NBO analysis) displays a significantly enriched contribution from 7p and 6d orbitals compared to **2** (Tables S22 and S23).

The *ab initio* CAS(3,12) computed $g_{zz}$ axis of KD1 lies along the $C_3$ axis (Figures 1 and S19a), and the three ground KDs generated from the $^6H_{5/2}$ state of **5** spans up to 1933.3 cm$^{-1}$. Further, the transverse anisotropy of the first two KDs is very small (Table 2), contrary to the uranium analogue. The largest $m_J$ of Pu(III) ($|\pm 5/2\rangle$) possesses prolate electron density (see Figures 8a and S20 and S21 for 5f and 6d orbitals), while the lowest $m_J$ ($|\pm 1/2\rangle$) of U(III) possesses prolate electron density, which implies that a suitable metal ion is required to produce potential SMM in a three-coordinate pyramidal geometry. The developed mechanism of magnetization relaxation reveals that the ground, first, and second excited KDs consist of $m_J = |\pm 5/2\rangle$, $|\pm 3/2\rangle$, and $|\pm 1/2\rangle$ states, respectively, and this quenches the QTM and TA-QTM for magnetization relaxation (Table 2, Figure 8b). This is analogous to Sm(III) in lanthanide complexes that stabilizes the largest $m_J$ state as the ground state with a strong equatorial ligand.[48] In the second excited KD, the large transverse anisotropy reinforces the magnetization relaxation via this state, setting a very large $U_{cal}$ value of 1933.3 cm$^{-1}$ for **5** (see Figure 8b for magnetization relaxation). Unfortunately, magnetic characterization has not been performed for this molecule. Unlike U(III), for the Pu(III) ion, the $5f^5 \rightarrow 5f^46d^1$ transition is expected to take place at a higher-energy window due to a large energy gap between 5f and 6d orbitals.[6i]

Furthermore, to study the effect of the out-of-plane shift in magnetic anisotropy, we have moved Pu(III) atom in **5** to the plane (**5′**, making $\tau = 0$, see Figures S19b and S22a). For this structure, the ground state $m_J = |\pm 5/2\rangle$ (see Figures S22b, S23, and S24) is similar to **5**, but the ligand field splitting is slightly larger ($\sim$300 cm$^{-1}$, Table 2), and the barrier height here is estimated to be 2252 cm$^{-1}$ (Table 2 and Figure S22b). While the planar geometry reduces the blocking barrier in **1**, the opposite behavior is found in **5** due to the stabilization of different ground $m_J$ states of U(III) vs Pu(III) ions. This delivers the idea that designing the ligand field of lanthanides according to prolate/oblate electron density can be extrapolated to actinides.

## 4. CONCLUSIONS

In summary, we performed DFT and *ab initio* CASSCF/CASPT2/NEVPT2 calculations to study suitable ligand fields for U(III)/Pu(III) SMMs among three-coordinate geometries.

Particularly, we have focused our attention on [U{N-(SiMe$_2^t$Bu)$_2$}$_3$] (**1**), [U{N(SiMe$_3$)$_2$}$_3$] (**2**), [U(NSi$^i$Pr$_2$)$_2$(I)] (**3**), [U(NHAr$^{iPr6}$)$_2$I] (**4**), and [Pu{N(SiMe$_3$)$_2$}$_3$] (**5**) complexes. The main conclusions derived from our calculations are mentioned below:

(i) To begin with, we have performed DFT-based AIM and NBO analysis on **1** and **2**, unveiling that the virtual low-lying 6d orbitals of uranium principally contribute to the metal—ligand bonding. It also takes part in the Pu/U···H—C$_\gamma$ and C$_\gamma$—Si···U/Pu agostic interaction along with the 5f orbitals in both the complexes. The metal—ligand covalency and the agostic interactions are larger in **1** than in **2**, whose contribution to anisotropy cannot be neglected.

(ii) We have performed method assessment using various *ab initio* methods such as CASSCF/CASPT2/NEVPT2 methods with available experimental observables such as $g$-tensors and susceptibility data. Our study reveals that extended CAS(3,12) active space captures the metal—ligand covalency and agostic interactions to some extent and improves the estimated magnetic characteristics substantially and hence is recommended for other systems.

(iii) Complexes **1** and **2** possess $m_J = |\pm 1/2\rangle$ ground state with a strong ground-state tunneling, rendering them unsuitable for SMMs. Magneto-structural correlations were developed based on the metal ion's out-of-plane shift, suggesting no substantial improvement in the magnetic properties. However, variation of point group symmetry leads to desired target, wherein a T-shaped $C_{2v}$ symmetry model yields excellent SMM characteristics.

(iv) Based on these ideas, two T-shaped U(III) complexes **3** and **4** reported in the literature were studied, and stabilization of $m_J = |\pm 9/2\rangle$ as the ground state is affirmed. Further CAS(3,12)SCF calculations predict the blocking barriers in the range of 900−1000 cm$^{-1}$ for these two complexes, and this is one of the largest known for any actinide-based SMMs if the Orbach mechanism is followed.

(v) Finally, we have extended our study to a reported pyramidal Pu(III) analogue of **2**, wherein stabilization of the largest $m_J = |\pm 5/2\rangle$ state is detected. As Pu(III) has a prolate electron density, the trigonal ligand field is found to be suitable, yielding a blocking barrier of more than 1900 cm$^{-1}$ if purely Orbach process is followed. The shift of Pu in the plane further increases the blocking barrier by

more than 300 cm$^{-1}$. Hence, the choice of the metal ion and the appropriate ligand field is key in determining the magnetic anisotropy in actinide SMMs.

## ■ ASSOCIATED CONTENT

### ⓈⒾ Supporting Information

The Supporting Information is available free of charge at https://pubs.acs.org/doi/10.1021/acs.inorgchem.1c02646.

CShM values of complexes **1** and **2**, spin density of ground spin free state, Laplacian of electron density and molecular graph from AIM analysis, donor−acceptor orbitals from NBO analysis, computed crystal field parameter and ground state $g_{zz}$ axis and relaxation mechanism from CASSCF calculation, 5f and 6d orbitals from CASSCF, fitted crystal field parameter from PHI, and comparison of fitted and experimental $\chi T$ (PDF)

## ■ AUTHOR INFORMATION

### Corresponding Author

**Gopalan Rajaraman** − *Department of Chemistry, Indian Institute of Technology Bombay, Mumbai 400076, India;* ⓞ orcid.org/0000-0001-6133-3026; Email: rajaraman@chem.iitb.ac.in

### Author

**Sourav Dey** − *Department of Chemistry, Indian Institute of Technology Bombay, Mumbai 400076, India*

Complete contact information is available at:
https://pubs.acs.org/10.1021/acs.inorgchem.1c02646

### Notes

The authors declare no competing financial interest.

## ■ ACKNOWLEDGMENTS
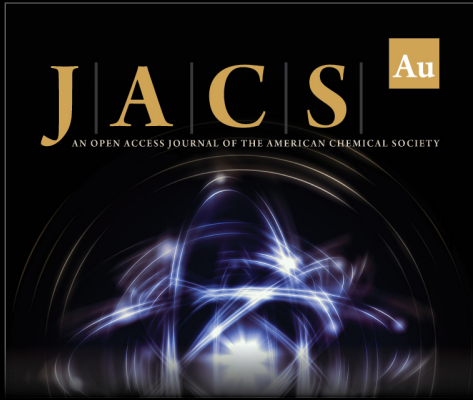
## ■ REFERENCES

(1) Gatteschi, D.; Sessoli, R.; Villain, J. *Molecular Nanomagnets*; Oxford University Press on Demand, 2006; Vol. 5.

(2) (a) Liddle, S. T.; van Slageren, J. Improving f-element single molecule magnets. *Chem. Soc. Rev.* **2015**, *44*, 6655−6669. (b) Canaj, A. B.; Dey, S.; Martí, E. R.; Wilson, C.; Rajaraman, G.; Murrie, M. Insight into D6h Symmetry: Targeting Strong Axiality in Stable Dysprosium (III) Hexagonal Bipyramidal Single-Ion Magnets. *Angew. Chem., Int. Ed.* **2019**, *131*, 14284−14289. (c) Canaj, A. B.; Dey, S.; Céspedes, O.; Wilson, C.; Rajaraman, G.; Murrie, M. There is nothing wrong with being soft: using sulfur ligands to increase axiality in a Dy (III) single-ion magnet. *Chem. Commun.* **2020**, *56*, 1533−1536. (d) Norre, M. S.; Gao, C.; Dey, S.; Gupta, S. K.; Borah, A.; Murugavel, R.; Rajaraman, G.; Overgaard, J. High-Pressure Crystallographic and Magnetic Studies of Pseudo-D 5 h Symmetric Dy (III) and Ho (III) Single-Molecule Magnets. *Inorg. Chem.* **2020**, *59*, 717−729. (e) Díaz-Ortega, I. F.; Herrera, J. M.; Dey, S.; Nojiri, H.; Rajaraman, G.; Colacio, E. The effect of the electronic structure and flexibility of the counteranions on magnetization relaxation in [Dy (L) 2 (H 2 O) 5] 3+(L = phosphine oxide derivative) pentagonal bipyramidal SIMs. *Inorg. Chem. Front.* **2020**, *7*, 689−699. (f) Gupta, S. K.; Rajeshkumar, T.; Rajaraman, G.; Murugavel, R. An air-stable Dy(iii) single-ion magnet with high anisotropy barrier and blocking temperature. *Chem. Sci.* **2016**, *7*, 5181−5191. (g) Krylov, D.S.; Liu, F.; Avdoshenko, S. M.; Spree, L.; Weise, B.; Waske, A.; Wolter, A. U. B.; Büchner, B.; Popov, A. A. Record-high thermal barrier of the relaxation of magnetization in the nitride clusterfullerene Dy 2 ScN@ C 80-I h. *Chem. Commun.* **2017**, *53*, 7901−

7904. (h) Liu, F.; Krylov, D. S.; Spree, L.; Avdoshenko, S. M.; Samoylova, N. A.; Rosenkranz, M.; Kostanyan, A.; Greber, T.; Wolter, A. U. B.; Büchner, B.; Popov, A. A. Single molecule magnet with an unpaired electron trapped between two lanthanide ions inside a fullerene. *Nat. Commun.* **2017**, *8*, No. 16098.

(3) (a) Goodwin, C. A. P.; Ortu, F.; Reta, D.; Chilton, N. F.; Mills, D. P. Molecular magnetic hysteresis at 60 kelvin in dysprosocenium. *Nature* **2017**, *548*, 439−442. (b) Guo, F.-S.; Day, B. M.; Chen, Y.-C.; Tong, M.-L.; Mansikkamäki, A.; Layfield, R. A. Magnetic hysteresis up to 80 kelvin in a dysprosium metallocene single-molecule magnet. *Science* **2018**, *362*, 1400−1403. (c) McClain, K. R.; Gould, C. A.; Chakarawet, K.; Teat, S. J.; Groshens, T. J.; Long, J. R.; Harvey, B. G. High-temperature magnetic blocking and magneto-structural correlations in a series of dysprosium (III) metallocenium single-molecule magnets. *Chem. Sci.* **2018**, *9*, 8492−8503. (d) Gould, C. A.; McClain, K. R.; Yu, J. M.; Groshens, T. J.; Furche, F.; Harvey, B. G.; Long, J. R. Synthesis and magnetism of neutral, linear metallocene complexes of terbium (II) and dysprosium (II). *J. Am. Chem. Soc.* **2019**, *141*, 12967−12973. (e) Canaj, A. B.; Dey, S.; Wilson, C.; Céspedes, O.; Rajaraman, G.; Murrie, M. Engineering macrocyclic high performance pentagonal bipyramidal Dy (iii) single-ion magnets. *Chem. Commun.* **2020**, *56*, 12037−12040.

(4) (a) Chen, Y.-C.; Liu, J.-L.; Ungur, L.; Liu, J.; Li, Q.-W.; Wang, L.-F.; Ni, Z.-P.; Chibotaru, L. F.; Chen, X.-M.; Tong, M.-L. Symmetry-supported magnetic blocking at 20 K in pentagonal bipyramidal Dy (III) single-ion magnets. *J. Am. Chem. Soc.* **2016**, *138*, 2829−2837. (b) Liu, J.-L.; Chen, Y.-C.; Tong, M.-L. Symmetry strategies for high performance lanthanide-based single-molecule magnets. *Chem. Soc. Rev.* **2018**, *47*, 2431−2453.

(5) Reta, D.; Kragskow, J. G. C.; Chilton, N. F. Ab Initio Prediction of High-Temperature Magnetic Relaxation Rates in Single-Molecule Magnets. *J. Am. Chem. Soc.* **2021**, *143*, 5943−5950.

(6) (a) Rinehart, J. D.; Long, J. R. Slow magnetic relaxation in a trigonal prismatic uranium (III) complex. *J. Am. Chem. Soc.* **2009**, *131*, 12558−12559. (b) Rinehart, J. D.; Meihaus, K. R.; Long, J. R. Observation of a secondary slow relaxation process for the field-induced single-molecule magnet U (H2BPz2) 3. *J. Am. Chem. Soc.* **2010**, *132*, 7572−7573. (c) Antunes, M. A.; Pereira, L. C.; Santos, I. C.; Mazzanti, M.; Marcalo, J.; Almeida, M. [U (TpMe2) 2 (bipy)]+: A Cationic Uranium (III) Complex with Single-Molecule-Magnet Behavior. *Inorg. Chem.* **2011**, *50*, 9915−9917. (d) Antunes, M. A.; Santos, I. C.; Bolvin, H.; Pereira, L. C.; Mazzanti, M.; Marçalo, J.; Almeida, M. Crystal structure diversity in the bis [hydrotris (3, 5-dimethylpyrazolyl) borate] iodouranium (III) complex: from neutral to cationic forms. *Dalton Trans.* **2013**, *42*, 8861−8867. (e) Coutinho, J. T.; Antunes, M. A.; Pereira, L. C.; Marçalo, J.; Almeida, M. Zero-field slow magnetic relaxation in a uranium (III) complex with a radical ligand. *Chem. Commun.* **2014**, *50*, 10262−10264. (f) Pereira, L. C.; Camp, C.; Coutinho, J. T.; Chatelain, L.; Maldivi, P.; Almeida, M.; Mazzanti, M. Single-molecule-magnet behavior in mononuclear homoleptic tetrahedral Uranium (III) complexes. *Inorg. Chem.* **2014**, *53*, 11809−11811. (g) Antunes, M. A.; Coutinho, J. T.; Santos, I. C.; Marçalo, J.; Almeida, M.; Baldoví, J. J.; Pereira, L. C.; Gaita-Ariño, A.; Coronado, E. A Mononuclear Uranium (IV) Single-Molecule Magnet with an Azobenzene Radical Ligand. *Chem. - Eur. J.* **2015**, *21*, 17817−17826. (h) Spivak, M.; Vogiatzis, K. D.; Cramer, C. J.; Graaf, Cd.; Gagliardi, L. Quantum Chemical Characterization of Single Molecule Magnets Based on Uranium. *J. Phys. Chem. A* **2017**, *121*, 1726−1733. (i) Gaggioli, C. A.; Gagliardi, L. Theoretical Investigation of Plutonium-Based Single-Molecule Magnets. *Inorg. Chem.* **2018**, *57*, 8098−8105. (j) Singh, S. K.; Cramer, C. J.; Gagliardi, L. Correlating Electronic Structure and Magnetic Anisotropy in Actinide Complexes [An (COT) 2], AnIII/IV= U, Np, and Pu. *Inorg. Chem.* **2020**, *59*, 6815−6825. (k) Meihaus, K. R.; Minasian, S. G.; Lukens, W. W., Jr.; Kozimor, S. A.; Shuh, D. K.; Tyliszczak, T.; Long, J. R. Influence of pyrazolate vs N-heterocyclic carbene ligands on the slow magnetic relaxation of homoleptic trischelate lanthanide (III) and uranium (III) complexes. *J. Am. Chem. Soc.* **2014**, *136*, 6056−6068. (l) Dey, S.; Rajaraman, G. In silico design of pseudo D 5h actinide based molecular

magnets: role of covalency in magnetic anisotropy. *J. Chem. Sci.* **2019**, *131*, No. 124. (m) Dey, S.; Velmurugan, G.; Rajaraman, G. How important is the coordinating atom in controlling magnetic anisotropy in uranium (III) single-ion magnets? A theoretical perspective. *Dalton Trans.* **2019**, *48*, 8976−8988. (n) Pereira, L. C.; Camp, C.; Coutinho, J. T.; Chatelain, L.; Maldivi, P.; Almeida, M.; Mazzanti, M. Single-molecule-magnet behavior in mononuclear homoleptic tetrahedral uranium(III) complexes. *Inorg. Chem.* **2014**, *53*, 11809−11811. (o) Mougel, V.; Chatelain, L.; Hermle, J.; Caciuffo, R.; Colineau, E.; Tuna, F.; Magnani, N.; de Geyer, A.; Pécaut, J.; Mazzanti, M. A Uranium-Based UO2+−Mn2+ Single-Chain Magnet Assembled trough Cation−Cation Interactions. *Angew. Chem., Int. Ed.* **2014**, *126*, 838−842. (p) Chatelain, L.; Pécaut, J.; Tuna, F.; Mazzanti, M. Heterometallic Fe2II−UV and Ni2II−UV Exchange-Coupled Single-Molecule Magnets: Effect of the 3 d Ion on the Magnetic Properties. *Chem. - Eur. J.* **2015**, *21*, 18038−18042. (q) Antunes, M. A.; Santos, I. C.; Bolvin, H.; Pereira, L. C.; Mazzanti, M.; Marcalo, J.; Almeida, M. Crystal structure diversity in the bis[hydrotris(3,5-dimethylpyrazolyl)-borate]iodouranium(III) complex: from neutral to cationic forms. *Dalton Trans.* **2013**, *42*, 8861−8867. (r) Coutinho, J. T.; Antunes, M. A.; Pereira, L. C.; Bolvin, H.; Marcalo, J.; Mazzanti, M.; Almeida, M. Single-ion magnet behaviour in [U(Tp(Me2))2I]. *Dalton Trans.* **2012**, *41*, 13568−13571. (s) Chatelain, L.; Tuna, F.; Pécaut, J.; Mazzanti, M. Synthesis and SMM behaviour of trinuclear versus dinuclear 3d−5f uranyl (v)−cobalt (ii) cation−cation complexes. *Dalton Trans.* **2017**, *46*, 5498−5502. (t) Moro, F.; Mills, D. P.; Liddle, S. T.; van Slageren, J. The inherent single-molecule magnet character of trivalent uranium. *Angew. Chem., Int. Ed.* **2013**, *125*, 3514−3517. (u) Goodwin, C. A.; Tuna, F.; McInnes, E. J.; Liddle, S. T.; McMaster, J.; Vitorica-Yrezabal, I. J.; Mills, D. P. [UIII {N (SiMe2tBu) 2} 3]: A Structurally Authenticated Trigonal Planar Actinide Complex. *Chem. - Eur. J.* **2014**, *20*, 14579−14583. (v) Seed, J. A.; Birnoschi, L.; Lu, E.; Tuna, F.; Wooles, A. J.; Chilton, N. F.; Liddle, S. T. Anomalous magnetism of uranium (IV)-oxo and -imido complexes reveals unusual doubly degenerate electronic ground states. *Chem* **2021**, *7*, 1666−1680.

(7) Rinehart, J. D.; Long, J. R. Slow magnetic relaxation in homoleptic trispyrazolylborate complexes of neodymium (III) and uranium (III). *Dalton Trans.* **2012**, *41*, 13572−13574.

(8) (a) Gaunt, A. J.; Enriquez, A. E.; Reilly, S. D.; Scott, B. L.; Neu, M. P. Structural characterization of Pu [N (SiMe3) 2] 3, a synthetically useful nonaqueous plutonium (iii) precursor. *Inorg. Chem.* **2008**, *47*, 26−28. (b) Clark, D. L.; Hecker, S. S.; Jarvinen, G. D.; Neu, M. P. Plutonium. In *The Chemistry of the Actinide and Transactinide Elements*; Springer, 2008; pp 813−1264. (c) Pellaud, B. Proliferation aspects of plutonium recycling. *C. R. Phys.* **2002**, *3*, 1067−1079. (d) Arnold, P. L.; Dutkiewicz, M. S.; Zegke, M.; Walter, O.; Apostolidis, C.; Hollis, E.; Pécharman, A. F.; Magnani, N.; Griveau, J. C.; Colineau, E.; et al. Subtle interactions and electron transfer between UIII, NpIII, or PuIII and uranyl mediated by the oxo group. *Angew. Chem.* **2016**, *128*, 12989−12993. (e) Fröhlich, D. R.; Kremleva, A.; Rossberg, A.; Skerencak-Frech, A.; Koke, C.; Krüger, S.; Rösch, N.; Panak, P. J. Combined EXAFS spectroscopic and quantum chemical study on the complex formation of Am (III) with formate. *Inorg. Chem.* **2017**, *56*, 6820−6829. (f) Liddle, S. T. The renaissance of non-aqueous uranium chemistry. *Angew. Chem., Int. Ed.* **2015**, *54*, 8604−8641.

(9) Higgins, R. F.; Tatebe, C. J.; Bart, S. C.; Shores, M. P. Excited-state effects on magnetic properties of U(iii) and U(iv) pyrazolylborate complexes. *Chem. Commun.* **2019**, *55*, 10611−10614.

(10) Mazzanti, M. Uranium memory. *Nat. Chem.* **2011**, *3*, 426−427.

(11) Autillo, M.; Islam, M. A.; Jung, J.; Pilmé, J.; Galland, N.; Guerin, L.; Moisy, P.; Berthon, C.; Tamain, C.; Bolvin, H. Crystallographic structure and crystal field parameters in the [An IV (DPA) 3] 2− series, An= Th, U, Np, Pu. *Phys. Chem. Chem. Phys.* **2020**, *22*, 14293−14308.

(12) (a) Stewart, J. L.; Andersen, R. A. Trivalent uranium chemistry: molecular structure of [(Me3Si) 2N] 3U. *Polyhedron* **1998**, *17*, 953−958. (b) Andersen, R. A.; Zalkin, A.; Templeton, D. H. Crystal and molecular structure of hydridotris [bis (trimethylsilyl) amido] uranium (IV). *Inorg. Chem.* **1981**, *20*, 622−623. (c) Van der Sluys, W. G.; Burns, C. J.; Sattelberger, A. P. First example of a neutral homoleptic uranium

alkyl. Synthesis, properties, and structure of U [CH (SiMe3) 2] 3. *Organometallics* **1989**, *8*, 855−857.

(13) (a) Goodwin, C. A. P.; Tuna, F.; McInnes, E. J. L.; Mills, D. P. Exploring Synthetic Routes to Heteroleptic UIII, UIV, and ThIVBulky Bis(silyl)amide Complexes. *Eur. J. Inorg. Chem.* **2018**, *2018*, 2356−2362. (b) Boreen, M. A.; Lussier, D. J.; Skeel, B. A.; Lohrey, T. D.; Watt, F. A.; Shuh, D. K.; Long, J. R.; Hohloch, S.; Arnold, J. Structural, Electrochemical, and Magnetic Studies of Bulky Uranium (III) and Uranium (IV) Metallocenes. *Inorg. Chem.* **2019**, *58*, 16629−16641.

(14) Aquilante, F.; Autschbach, J.; Carlson, R. K.; Chibotaru, L. F.; Delcey, M. G.; De Vico, L.; Fdez Galván, I.; Ferré, N.; Frutos, L. M.; Gagliardi, L.; et al. Molcas 8: New capabilities for multiconfigurational quantum chemical calculations across the periodic table. *J. Comput. Chem.* **2016**, *37*, 506−541.

(15) Roos, B. O.; Veryazov, V.; Widmark, P.-O. Relativistic atomic natural orbital type basis sets for the alkaline and alkaline-earth atoms applied to the ground-state potentials for the corresponding dimers. *Theor. Chem. Acc.* **2004**, *111*, 345−351.

(16) Wolf, A.; Reiher, M.; Hess, B. A. The generalized Douglas−Kroll transformation. *J. Chem. Phys.* **2002**, *117*, 9215−9226.

(17) Aquilante, F.; Malmqvist, P.-Å.; Pedersen, T. B.; Ghosh, A.; Roos, B. O. Cholesky decomposition-based multiconfiguration second-order perturbation theory (CD-CASPT2): application to the spin-state energetics of CoIII (diiminato)(NPh). *J. Chem. Theory Comput.* **2008**, *4*, 694−702.

(18) Zobel, J. P.; Nogueira, J. J.; González, L. The IPEA dilemma in CASPT2. *Chem. Sci.* **2017**, *8*, 1482−1499.

(19) Malmqvist, P. Å.; Roos, B. O.; Schimmelpfennig, B. The restricted active space (RAS) state interaction approach with spin−orbit coupling. *Chem. Phys. Lett.* **2002**, *357*, 230−240.

(20) Ungur, L.; Van den Heuvel, W.; Chibotaru, L. F. Ab initio investigation of the non-collinear magnetic structure and the lowest magnetic excitations in dysprosium triangles. *New J. Chem.* **2009**, *33*, 1224.

(21) Neese, F. *ORCA—An Ab Initio, DFT and Semiempirical Electronic Structure Package*, Ver. 4.0.1; Max Planck Institute for Chemical Energy Conversion: Mülheim, Germany, 2017.

(22) Maurice, R.; Bastardis, R.; Graaf, Cd.; Suaud, N.; Mallah, T.; Guihery, N. Universal theoretical approach to extract anisotropic spin hamiltonians. *J. Chem. Theory Comput.* **2009**, *5*, 2977−2984.

(23) Jung, J. C. A. O.; Islam, M. A.; Pecoraro, V. L.; Mallah, T.; Berthon, C.; Bolvin, H. *Derivation of Lanthanide Series Crystal Field Parameters From First Principles*; 0947-6539; Los Alamos National Lab. (LANL): Los Alamos, NM, 2019.

(24) (a) Frisch, M. J.; Trucks, G. W.; Schlegel, H. B.; Scuseria, G. E.; Robb, M. A.; Cheeseman, J. R.; Scalmani, G.; Barone, V.; Mennucci, B.; Petersson, G. A.; Nakatsuji, H.; Caricato, M.; Li, X.; Hratchian, H. P.; Izmaylov, A. F.; Bloino, J.; Zheng, G.; Sonnenberg, J. L.; Hada, M.; Ehara, M.; Toyota, K.; Fukuda, R.; Hasegawa, J.; Ishida, M.; Nakajima, T.; Honda, Y.; Kitao, O.; Nakai, H.; Vreven, T.; Montgomery, J. A., Jr.; Peralta, J. E.; Ogliaro, F.; Bearpark, M.; Heyd, J. J.; Brothers, E.; Kudin, K. N.; Staroverov, V. N.; Kobayashi, R.; Normand, J.; Raghavachari, K.; Rendell, A.; Burant, J. C.; Iyengar, S. S.; Tomasi, J.; Cossi, M.; Rega, N.; Millam, J. M.; Klene, M.; Knox, J. E.; Cross, J. B.; Bakken, V.; Adamo, C.; Jaramillo, J.; Gomperts, R.; Stratmann, R. E.; Yazyev, O.; Austin, A. J.; Cammi, R.; Pomelli, C.; Ochterski, J. W.; Martin, R. L.; Morokuma, K.; Zakrzewski, V. G.; Voth, G. A.; Salvador, P.; Dannenberg, J. J.; Dapprich, S.; Daniels, A. D.; Farkas, O.; Foresman, J. B.; Ortiz, J. V.; Cioslowski, J.; Fox, D. J. *Gaussian 09*, Revision A.02; Gaussian, Inc.: Wallingford, CT, 2009. (b) Becke, A. D. Density-functional thermochemistry. III. The role of exact exchange. *J. Chem. Phys.* **1993**, *98*, 5648−5652.

(25) (a) Küchle, W.; Dolg, M.; Stoll, H.; Preuss, H. Energy-adjusted pseudopotentials for the actinides. Parameter sets and test calculations for thorium and thorium monoxide. *J. Chem. Phys.* **1994**, *100*, 7535−7542. (b) Cao, X.; Dolg, M. Segmented contraction scheme for small-core actinide pseudopotential basis sets. *J. Mol. Struct.: THEOCHEM* **2004**, *673*, 203−209.

(26) (a) Schäfer, A.; Horn, H.; Ahlrichs, R. Fully optimized contracted Gaussian basis sets for atoms Li to Kr. *J. Chem. Phys.* **1992**, *97*, 2571−2577. (b) Schäfer, A.; Huber, C.; Ahlrichs, R. Fully optimized contracted Gaussian basis sets of triple zeta valence quality for atoms Li to Kr. *J. Chem. Phys.* **1994**, *100*, 5829−5835.

(27) Biegler-König, F.; Schönbohm, J. Update of the AIM2000-program for atoms in molecules. *J. Comput. Chem.* **2002**, *23*, 1489−1494.

(28) Weinhold, F.; Landis, C. R. *Valency and Bonding: A Natural Bond Orbital Donor-Acceptor Perspective*; Cambridge University Press, 2005.

(29) Llunell, M.; Casanoval, D.; Cirera, J.; Alemany, P.; Alvarez, S. *SHAPE*, v2.1; University of Barcelona and The Hebrew University of Jerusalem: Barcelona and Jersalem, 2013.

(30) (a) Beekmeyer, R.; Kerridge, A. Assessing covalency in cerium and uranium hexachlorides: A correlated wavefunction and density functional theory study. *Inorganics* **2015**, *3*, 482−499. (b) Kerridge, A. Oxidation state and covalency in f-element metallocenes (M= Ce, Th, Pu): a combined CASSCF and topological study. *Dalton Trans.* **2013**, *42*, 16428−16436. (c) Vlaisavljevich, B.; Miró, P.; Cramer, C. J.; Gagliardi, L.; Infante, I.; Liddle, S. T. On the Nature of Actinide−and Lanthanide−Metal Bonds in Heterobimetallic Compounds. *Chem. - Eur. J.* **2011**, *17*, 8424−8433. (d) Bi, Y.-T.; Li, L.; Guo, Y.-R.; Pan, Q.-J. Heterobimetallic Uranium−Nickel/Palladium/Platinum Complexes of Phosphinoaryl Oxide Ligands: A Theoretical Probe for Metal−Metal Bonding and Electronic Spectroscopy. *Inorg. Chem.* **2019**, *58*, 1290−1300.

(31) Bader, R. *A Quantum Theory*; Clarendon: Oxford, 1990.

(32) Popov, A. A.; Avdoshenko, S. M.; Pendás, A. M.; Dunsch, L. Bonding between strongly repulsive metal atoms: an oxymoron made real in a confined space of endohedral metallofullerenes. *Chem. Commun.* **2012**, *48*, 8031−8050.

(33) Singh, S. K.; Pandey, B.; Velmurugan, G.; Rajaraman, G. Key role of higher order symmetry and electrostatic ligand field design in the magnetic relaxation of low-coordinate Er (iii) complexes. *Dalton Trans.* **2017**, *46*, 11913−11924.

(34) Gupta, T.; Velmurugan, G.; Rajeshkumar, T.; Rajaraman, G. Role of Lanthanide-Ligand bonding in the magnetization relaxation of mononuclear single-ion magnets: A case study on Pyrazole and Carbene ligated LnIII (Ln= Tb, Dy, Ho, Er) complexes. *J. Chem. Sci.* **2016**, *128*, 1615−1630.

(35) Long, J.; Guari, Y.; Ferreira, R. A. S.; Carlos, L. D.; Larionova, J. Recent advances in luminescent lanthanide based Single-Molecule Magnets. *Coord. Chem. Rev.* **2018**, *363*, 57−70.

(36) Hay, P. J.; Martin, R. L. Theoretical studies of the structures and electronic properties of U (NH2) 3 and Np (NH2) 3. *J. Alloys Compd.* **1994**, *213−214*, 196−198.

(37) Mansell, S. M.; Perandones, B. F.; Arnold, P. L. New UIII and UIV silylamides and an improved synthesis of NaN(SiMe2R)2 (R = Me, Ph). *J. Organomet. Chem.* **2010**, *695*, 2814−2821.

(38) (a) Chilton, N. F.; Anderson, R. P.; Turner, L. D.; Soncini, A.; Murray, K. S. PHI: a powerful new program for the analysis of anisotropic monomeric and exchange-coupled polynuclear d- and f-block complexes. *J. Comput. Chem.* **2013**, *34*, 1164−1175. (b) Rudowicz, C. Transformation relations for the conventional Okq and normalised O'kq Stevens operator equivalents with k= 1 to 6 and-k⩽ q⩽ k. *J. Phys. C: Solid State Phys.* **1985**, *18*, 1415. (c) Hutchings, M. *Solid State Physics: Advances in Research and Applications*; Seitz, F.; Turnbull, B., Eds.; Academic: New York, 1965.

(39) Benelli, C.; Gatteschi, D. *Introduction to Molecular Magnetism: From Transition Metals to Lanthanides*; John Wiley & Sons, 2015.

(40) Neese, F. Software update: the ORCA program system, version 4.0. *Wiley Interdiscip. Rev.: Comput. Mol. Sci.* **2018**, *8*, No. e1327.

(41) Baldoví, J. J.; Cardona-Serra, S.; Clemente-Juan, J. M.; Coronado, E.; Gaita-Ariño, A. Modeling the properties of uranium-based single ion magnets. *Chem. Sci.* **2013**, *4*, 938−946.

(42) Gupta, S. K.; Rajeshkumar, T.; Rajaraman, G.; Murugavel, R. An unprecedented zero field neodymium (III) single-ion magnet based on a phosphonic diamide. *Chem. Commun.* **2016**, *52*, 7168−7171.

(43) Singh, S. K.; Gupta, T.; Ungur, L.; Rajaraman, G. Magnetic Relaxation in Single-Electron Single-Ion Cerium (III) Magnets: Insights from Ab Initio Calculations. *Chem. - Eur. J.* **2015**, *21*, 13812.

(44) McAdams, S. G.; Ariciu, A.-M.; Kostopoulos, A. K.; Walsh, J. P.; Tuna, F. Molecular single-ion magnets based on lanthanides and actinides: Design considerations and new advances in the context of quantum technologies. *Coord. Chem. Rev.* **2017**, *346*, 216−239.

(45) Billow, B. S.; Livesay, B. N.; Mokhtarzadeh, C. C.; McCracken, J.; Shores, M. P.; Boncella, J. M.; Odom, A. L. Synthesis and Characterization of a Neutral U(II) Arene Sandwich Complex. *J. Am. Chem. Soc.* **2018**, *140*, 17369−17373.

(46) Jung, J.; Atanasov, M.; Neese, F. Ab Initio Ligand-Field Theory Analysis and Covalency Trends in Actinide and Lanthanide Free Ions and Octahedral Complexes. *Inorg. Chem.* **2017**, *56*, 8802−8816.

(47) Magnani, N.; Colineau, E.; Griveau, J. C.; Apostolidis, C.; Walter, O.; Caciuffo, R. A plutonium-based single-molecule magnet. *Chem. Commun.* **2014**, *50*, 8171−8173.

(48) Rinehart, J. D.; Long, J. R. Exploiting single-ion anisotropy in the design of f-element single-molecule magnets. *Chem. Sci.* **2011**, *2*, 2078−2085.